



# Research on chip formation mechanism and surface morphology of particle-reinforced metal matrix composites

Yuxin Fang<sup>1,2</sup> · Youqiang Wang<sup>1,2</sup> · Ping Zhang<sup>3</sup> · Heng Luo<sup>1,2</sup>

Received: 20 May 2021 / Accepted: 20 August 2021 / Published online: 3 September 2021  
© The Author(s), under exclusive licence to Springer-Verlag London Ltd., part of Springer Nature 2021

## Abstract

In this paper, a finite element (FE) cutting model for particle-reinforced metal matrix composites (PRMMCs) considering material damage was developed to predict SiC particle failure, cutting forces, and machined surface topography in SiC<sub>p</sub>/Al composite machining, and to analyze the dynamic mechanisms of chip formation and particle failure evolution. The validity of the simulation model was verified by comparing the simulation results with the cutting forces and surface topography obtained from the milling machining experiments. It was found that complex stress-strain fields exist in SiC<sub>p</sub>/Al composites with mesoscopic non-homogeneous structures, and alternating reticulation of tensile and compressive stress between particles was observed; particle failure due to tool-workpiece interaction exists in both direct and indirect ways; particle failure and local chip deformation during machining affect surface topography and chip shaping, resulting in serrated chips, pitting on the machined surface, and residual particle fragments.

**Keywords** Finite element simulation · Particle-reinforced metal matrix composites · Chip formation mechanism · Machined surface topography

## 1 Introduction

Particle-reinforced metal matrix composites (PRMMCs), as represented by SiC<sub>p</sub>/Al composites, have been widely used in automobile, aerospace, and electronic packaging applications for their high specific strength and specific stiffness, good heat conductivity, and low coefficient of expansion [1–3]. While the addition of particle reinforcement greatly improves the overall properties of composites, however, it also introduces undesirable problems such as severe tool wear and poor surface machining quality. In response to this

problem, the machinability of PRMMCs has been extensively researched in order to develop better machining techniques.

The experiment is a powerful approach to investigate the machinability of PRMMCs, yet it is difficult to directly observe the dynamic chip formation process in machining with experiments [4, 5]. To solve this problem, finite element (FE) technique has been widely used [6, 7]. The multiphase (MP) modeling has been widely used to study the complex tool-particle interaction during the machining of PRMMCs [8, 9]. The mechanical property of SiC<sub>p</sub>/Al composites is affected by the size and volume fraction of the silicon carbide (SiC) particles [10–13]. Moreover, it was found that composites prepared from SiC particles with fewer sharp corners possess better ductility [14, 15], and less sharp-edged SiC particles are closer to spherical shape, which provides a meaningful reference for the use of round SiC particles in FE modeling, as they are already widely used in the simulation of PRMMCs.

Regarding the machinability of SiC<sub>p</sub>/Al composites, numerous studies [16–18] have shown that cutting parameters, tool geometry, and preparation parameters of the composites affect the cutting force, cutting temperature, chip morphology, and surface quality. The addition of the SiC particle reinforcement phase leads to complex tool-particle interactions during machining, and further studies found that the mesoscopic non-

✉ Youqiang Wang  
wyq1970301@126.com

✉ Ping Zhang  
18661660729@163.com

<sup>1</sup> School of Mechanical and Automotive Engineering, Qingdao University of Technology, Qingdao 266525, China

<sup>2</sup> Key Lab of Industrial Fluid Energy Conservation and Pollution Control, Ministry of Education, Qingdao 266520, China

<sup>3</sup> School of Mechanical and Power of Engineering, East China University of Science and Technology, Shanghai 200237, China

homogeneous structure of PRMMCs causes inhomogeneous stress-strain during machining [19–21]; and the random contact between the cutting tool edge and particles during machining will lead to multiple relative positions between them, which has important effects on particle damage, tool wear, and damage to the machined surface [22–26]. Although many scholars have conducted simulation studies on the machinability of  $\text{SiC}_p/\text{Al}$  composites, no intensive research has been conducted on the chip formation mechanism and the formation of surface defects which are considering particle failure, and the details of the stress-strain field in machining are still less studied, so the investigation of the removal process of composites needs to be further explored.

Compared to homogeneous materials, PRMMCs have complex tool-particle interactions in machining. Given the extremely high hardness of  $\text{SiC}$  particles, poor surface quality and severe tool wear constitute two big challenges for the machining of  $\text{SiC}_p/\text{Al}$  composites. In this paper, the finite element method was applied to simulate the dynamic chip formation process of  $\text{SiC}_p/\text{Al}$  composites to reveal the chip formation mechanism and the evolution of surface defects, and the validity was verified by comparing the chip shape, cutting force, and surface topography obtained after milling the composite material. This is of great significance to enhance the understanding of the deformation process of this material, improve the machinability of PRMMCs, and promote the application of this material.

## 2 Finite element modeling process

Figure 1 shows the microstructure of the  $\text{SiC}_p/\text{Al}$  composite. It is certain that the addition of the reinforcing phase induces a more complex stress-strain field in the machining, and the single closure theory is not suitable for studying complex-structured PRMMCs, so finite element computational micromechanics (FECM) has been widely used to simulate

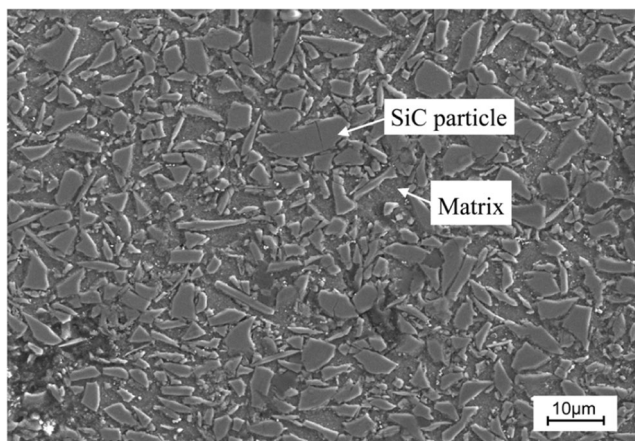


Fig. 1 Microstructure of  $\text{SiC}_p/\text{Al}$  composites

their chip separation process [27–30]. With this strategy, not only the overall response of composites can be derived, but also details of stress and strain fields and tool-workpiece interactions in the microstructure of multiphase materials can be studied, so that the chip formation mechanism of the composites can be investigated in detail.

### 2.1 Geometric model

In this study, the particles were assumed to be uniformly distributed inside the composite, and the three-dimensional milling model was simplified to two dimensions by adopting the assumptions of Teng [16, 17], and the two-dimensional  $\text{SiC}_p/\text{Al}$  composite microscopic milling modeling was established by using ABAQUS finite element simulation software and composite construction scripts, as shown in Fig. 2. The size of the workpiece was  $0.5 \times 0.2$  mm, and the  $\text{SiC}$  particles were simplified as round with a volume fraction of 45%. The size and location distribution of the particles were prepared using a python script, i.e., a normal distribution algorithm was used to generate a list of particle sizes with a mean of 5  $\mu\text{m}$  in the interval [3.75, 6.25]  $\mu\text{m}$  and to distribute them randomly in the model. Other model setting parameters are shown in Table 1.

### 2.2 Material constitutive model

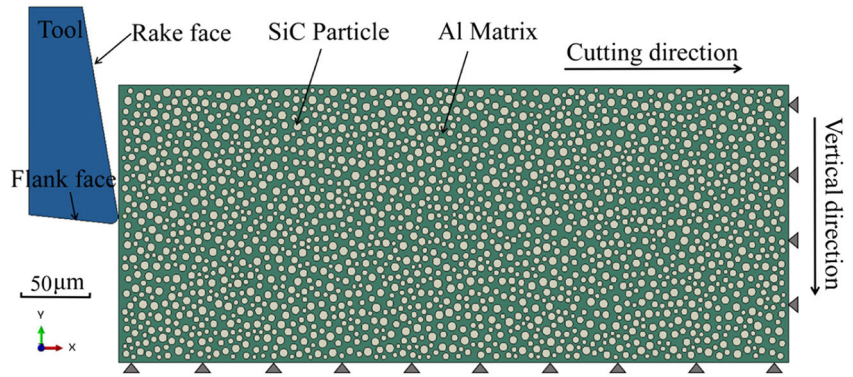
The typical stress-strain response of the metal shown in Fig. 3 was adopted to describe the deformation and failure process of the material in the finite element model. The OA section represents the elastic deformation stage; the AB section represents the plastic yield and strain hardening stage; the OABC section of the curve represents the stress-strain response when the material is undamaged; point B corresponds to the damage initiation point, after which the load bearing capacity decreases and enters the stage of damage evolution; the BD segment of the curve represents the damage evolution stage, where the stress-strain response is governed by the stiffness degradation in the region of strain localization; the point D corresponds to the material fracture point, at which the element will be removed from the calculation.

The Johnson-Cook [31, 32] constitutive equation, as shown in Eq. (1), which well characterizes the viscoplastic deformation of materials under high temperature, high strain,

Table 1 Model parameters

Cutting speed ( $v_c$ (m/min))	500
Feed rate ( $f$ (mm))	0.1
Rake angle ( $^\circ$ )	10
Flank angle ( $^\circ$ )	6
Average particle size ( $\mu\text{m}$ )	5

**Fig. 2** Two-dimensional cutting model of SiC<sub>p</sub>/Al composites



and high strain rate conditions, is widely used in simulating the cutting process of metal materials. The constitutive parameters are shown in Table 2 [32], and the remaining properties parameters are shown in Table 3 [32, 33].

$$\sigma = \left[ A + B \left( \bar{\epsilon}^{pl} \right)^n \right] \left[ 1 + C \ln \left( \frac{\dot{\bar{\epsilon}}^{pl}}{\dot{\epsilon}_0^*} \right) \right] \left[ 1 - \left( \frac{T - T_0}{T_{melt} - T_0} \right)^m \right] \quad (1)$$

where  $A$  is the yield strength under quasi-static conditions,  $B$  is the hardening modulus,  $\bar{\epsilon}^{pl}$  is the equivalent plastic strain,  $n$  is the hardening coefficient,  $C$  is the strain rate sensitivity coefficient,  $\dot{\bar{\epsilon}}^{pl}$  is the plastic strain rate,  $\dot{\epsilon}_0^*$  is the reference plastic strain rate,  $T$  is the workpiece current temperature,  $T_{melt}$  is the material melting temperature,  $T_0$  is the room temperature, and  $m$  is the thermal softening coefficient.

### 2.3 Chip separation criteria

The chip-workpiece separation in the cutting simulation is based on the deletion of the element, which can be described by a damage initiation criterion and a damage evolution criterion. The damage initiation of the matrix material was described by Johnson-Cook damage model [32], as shown in Eq. (2).

$$\bar{\epsilon}_0^p = \left[ d_1 + d_2 \exp \left( d_3 \frac{\sigma_p}{\sigma_{Mises}} \right) \right] \left[ 1 + d_4 \ln \left( \frac{\dot{\bar{\epsilon}}^{pl}}{\dot{\epsilon}_0^*} \right) \right] \left[ 1 + d_5 \left( \frac{T - T_0}{T_{melt} - T_0} \right) \right] \quad (2)$$

where  $\sigma_p$  stands for compressive stress,  $\sigma_{Mises}$  represents Mises stress, and  $d_1 \sim d_5$  are material failure parameters. The physical meanings of other parameters are the same as defined in Eq. (1). The material failure parameters are shown in Table 4.

In Abaqus, the criterion for determining that an element meets the damage initiation is that the damage parameter exceeds 1, as shown in Eq. (3).

$$\omega = \sum \frac{\Delta \bar{\epsilon}^p}{\bar{\epsilon}_0^p} \quad (3)$$

where  $\omega$  is the damage parameter,  $\Delta \bar{\epsilon}^p$  is the equivalent plastic strain increment, and  $\bar{\epsilon}_0^p$  is the equivalent plastic strain at the onset of damage.

The damage evolution law describes the degradation rate of the material stiffness after satisfying the damage initiation criterion, and the reduction in the stiffness factor is controlled by the damage variable. In the stage of damage evolution, the equivalent stress of the material is as follows:

$$\bar{\sigma} = (1 - D) \tilde{\sigma} \quad (4)$$

where  $D$  is the overall damage variable and  $\tilde{\sigma}$  is the undamaged stress tensor calculated in current increments.

To avoid the strong mesh dependence caused by strain localization, an exponential evolution criterion based on energy dissipation was used to describe the damage evolution

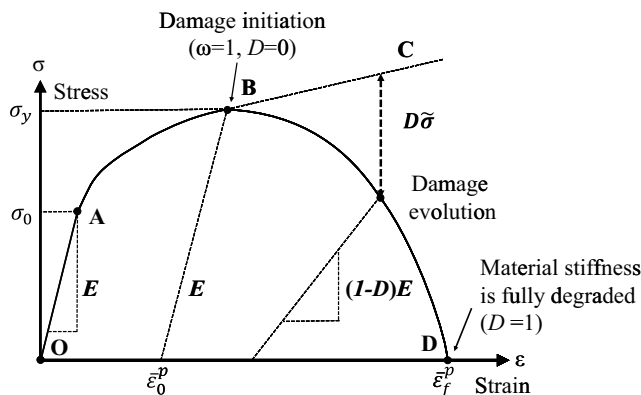


**Fig. 3** The stress-strain curve with progressive damage degradation

**Table 2** Johnson-Cook constitutive parameters of 2024Al

$A$ (MPa)	$B$ (MPa)	$C$	$m$	$n$	$T_0$ (K)	$T_{melt}$ (K)
369	684	0.0083	1.7	0.73	293	795

**Table 3** Material parameters

Materials	2024Al	SiC	PCD tool
Density (kg/m <sup>3</sup> )	2770	3130	4250
Young's modulus (GPa)	73	420	1174
Poisson's ratio	0.33	0.14	0.07
Thermal conductivity (W/(m K))	190	81	2100
Thermal expansion (°C <sup>-1</sup> )	2.1 × 10 <sup>-5</sup>	4.9 × 10 <sup>-6</sup>	4.0 × 10 <sup>-6</sup>
Thermal specific heat (J/(kg K))	875	427	525

behavior of the aluminum substrate material. The fracture energy based on the stress-displacement response is as follows:

$$G_f = \int_{\bar{\varepsilon}_0}^{\bar{\varepsilon}_f} L \bar{\sigma} d\bar{\varepsilon}^p = \int_0^{\bar{u}_f} \bar{\sigma} d\bar{u}^p \quad (5)$$

where  $L$  is the characteristic length of the element and  $\bar{u}^p$  and  $\bar{\sigma}$  are the equivalent plastic displacement and stress.

The exponential evolution of the overall damage variable  $D$  is expressed as:

$$D = 1 - \exp\left(-\int_0^{\bar{u}^p} \frac{\bar{\sigma}}{G_f} d\bar{u}^p\right) \quad (6)$$

The crack initiation and post-cracking behavior of SiC material were defined by the brittle cracking model. The Rankine criterion based on type I fracture was used to assess the crack initiation for SiC material, i.e., Eq. (7), when the maximum principal stress exceeds the ultimate strength of SiC materials, cracks develop and enter the post-cracking stage; the post-cracking behavior was described by a cracking criterion based on the fracture energy [34], in which the cracking stress decreases with increasing crack normal displacement until it reaches zero when the particle was fractured, and the crack normal displacement  $u_{n0}$  at fractured is expressed in Eq. (8).

$$\max(\sigma_1, \sigma_2, \sigma_3) = \sigma_b \quad (7)$$

$$u_{n0} = 2G_f / \sigma_b \quad (8)$$

**Table 4** Material failure parameters

Material	$d_1$	$d_2$	$d_3$	$d_4$	$d_5$
2024Al	0.0071	1.248	-1.142	0.147	0.1

In Eq. (7),  $\sigma_1$ ,  $\sigma_2$ , and  $\sigma_3$  are the principal stresses, and  $\sigma_b=1000$  Mpa [35, 36] is the ultimate strength of the SiC material. In Eq. (8),  $G_f^I$  is the type I fracture energy.

The initiation of cracking in the brittle cracking model is based solely on Mode I fracture, but Mode II fracture also occurs during the post-cracking behavior of SiC, so a shear retention model was implemented to describe the variation of shear modulus with crack opening strain during the post-cracking process [37], as shown in Eq. (9):

$$G_C = \rho(e_{mn}^{ck}) G = \left(1 - \frac{e_{mn}^{ck}}{e_{max}^{ck}}\right)^p G \quad (9)$$

where  $G_C$  is shear modulus of post-cracking process,  $G$  is the shear modulus of the uncracked material,  $\rho(e_{mn}^{ck})$  is the shear retention factor,  $e_{mn}^{ck}$  is the crack opening strain, and  $p(=1)$  and  $e_{max}^{ck}$  ( $=0.001$ ) [38] are material parameters.

To describe the frictional characteristics of the tool-chip interface, Zorev's stick-slip friction model [39] was adopted. The stress and temperature between the tool-chip interface change sharply from the cutting tool edge to the chip outflow point, so the sticking friction will appear near the cutting tool edge, and the equivalent shear stress is the ultimate shear stress of the material, as shown in Eq. (10); and in the contact zone far from the cutting tool edge, the contact stress and temperature fall, the sticking friction changes to sliding friction, and the equivalent shear stress is calculated according to Eq. (11).

$$\tau = \tau_{lim} \quad \text{when} \quad \mu\sigma_c \geq \tau_{lim} \quad (10)$$

$$\tau = \mu\sigma_c \quad \text{when} \quad \mu\sigma_c < \tau_{lim} \quad (11)$$

where  $\tau$  is the equivalent shear stress on the tool-work interface,  $\sigma_c$  is the normal stress,  $\mu$  ( $=0.35$ ) [40] is the coefficient of friction, and  $\tau_{lim}$  is the limiting shear stress of the workpiece material.

## 2.4 Meshing and boundary conditions

The model was meshed using CPE4RT elements with a free meshing strategy. The lower and left ends of the workpiece were restricted to all degrees of freedom to simulate boundary conditions in the cutting. Considering the high interfacial bonding strength of SiC to the metal matrix [41, 42], the SiC particles were set to be tied to the aluminum matrix in the model. The tool was set as rigid without regard to deformation and wear due to the low feed rate, high hardness of the PCD tool, and short cutting time.

### 3 Results and discussion

#### 3.1 Chip formation process

The addition of the reinforcing phase results in an inhomogeneous structure, which has a non-negligible effect on the stress fields. Most scholars used Mises stress to characterize the stress field, but as the equivalent stress, it cannot identify the specifics of the tension-compression stress. To solve this problem, the Max principal (abs) stress (the stress of the principal stress with the largest absolute value) was chosen to describe the stress field during chip formation, as shown in Fig. 4.

As illustrated by Fig. 4a, compressive stress exists near the cutting tool edge at the beginning of the contact, and tensile stress gradually appears in the inward transition, with an alternating distribution of compressive and tensile stresses within the material. The elastic-plastic deformation of the matrix is not uniform in different directions due to the presence of particles, which can cause tensile or compressive stresses between the particles (Fig. 4a–b), and the extrusion of the composites by the tool during machining shortens the transverse distance between the particles inducing compressive stresses, which can lead to particle fracture when the stress concentration caused by the matrix deformation exceeds the strength limit of the SiC material (Fig. 4c). With the tool advance, the material deformation becomes more severe, and continuously broken particles cause small cracks and holes to appear within the composites (Fig. 4d), and extreme shear deformation in the primary shear zone during chip formation causes a large number of particles to fracture (Fig. 4e). It can be seen that the chip formation of SiC<sub>p</sub>/Al composites involves not only local shear deformation of the matrix material, but also the expansion of microcracks and holes induced by particle fracture, which make it easy to segment the chips along the primary shear surface and display serrated shapes.

The SiC<sub>p</sub>/Al composite was milled according to the parameters in Table 1, and the chips were collected for inlaying and polishing. The microscopic morphology of the chips was obtained as shown in Fig. 5, where it can be seen that the chips are serrated and that local shear deformation zones exist, leading to periodic chip fracture (Fig. 5b–d). The particles in the local shear deformation zone are finer than those outside the zone, indicating that particles in the local shear deformation zone fracture more frequently and that fracture of particles inside the chip makes it easier to produce and expand microcracks to fracture the chip (Fig. 5d).

The peak cutting forces obtained from simulation and experiment are shown in Fig. 6. The peak cutting forces predicted by simulation in the *X* and *Y* directions are 302.25 N and 70.24 N, respectively, while the peak cutting forces obtained by experiment are 321.7 N and 77.3 N. The error between predicted and experimental cutting forces is less than 15%, which can reflect the accuracy of the finite element model.

#### 3.2 Analysis of the stress-strain field

The stress field of the composites during machining shows an interleaved reticulation of tensile and compressive stresses, as shown in Fig. 4. The reinforcing particles have a restraining effect on composites deformation and stress propagation, and there are different relative positions between the randomly distributed particles, making the tensile and compressive deformation of the matrix material caused by tool extrusion to be more significant between the particles, so that the stress fields between adjacent particles are obviously different, as shown in Fig. 7a–b. Here, we proposed three types of inter-particle relative position distributions, summarized as shown in Fig. 7c: (a) particles with longitudinal relative position (particles A–C–F, particles B–D–G, particles E–H), (b) particles with transverse relative position (particles A–B–E, particles C–D, particles F–G–H), and (c) particles with oblique relative position (particles C–B, particles D–E), and these three relative position distributions are prevalent in a large number of randomly distributed particles.

During machining, the extrusion of the tool on the composites will cause the longitudinal elongation of the matrix material along the cutting layer thickness direction, subjecting the longitudinally distributed particles to tensile stress, while the matrix material will be compressed along the cutting speed direction, subjecting the transversely distributed particles to compressive stress; meanwhile, shear deformation of the matrix material will cause the particles along the oblique direction to have small displacements and lead to compression or tension generation. When stress fields between particles with different relative position distributions are interconnected, the tensile and compressive stresses will show alternate distributions. When the stress concentration on the particles exceeds the strength limit of the SiC material, it leads to particle fracture, as evidenced by the fact that particle failure occurs mainly along the stress propagation path (Fig. 4d–e).

To further analyze the shear deformation pattern and chip formation mechanism of the composites during machining, the LE max principal (abs) strain field (corresponding to the Max principal (abs) stress) in the composites was selected as shown in Fig. 8.

The alternate reticulation of tensile and compressive strains was visible in the strain field in Fig. 8. In the process of tool embedding in the composites, the extrusion of the tool on the composites caused severe compressive deformation near the tip of the tool, resulting in compressive strain between the particles, and the strain field tended to expand in the direction of the cutting speed (Fig. 8a). With the further tool movement, some of the particles affected by matrix material deformation began to fracture (Fig. 8b–c); as the deformation increased, severe shear deformation occurred in the main shear zone, and a large number of particles in the deformation zone fractured due to the compound action of tensile and compressive strains

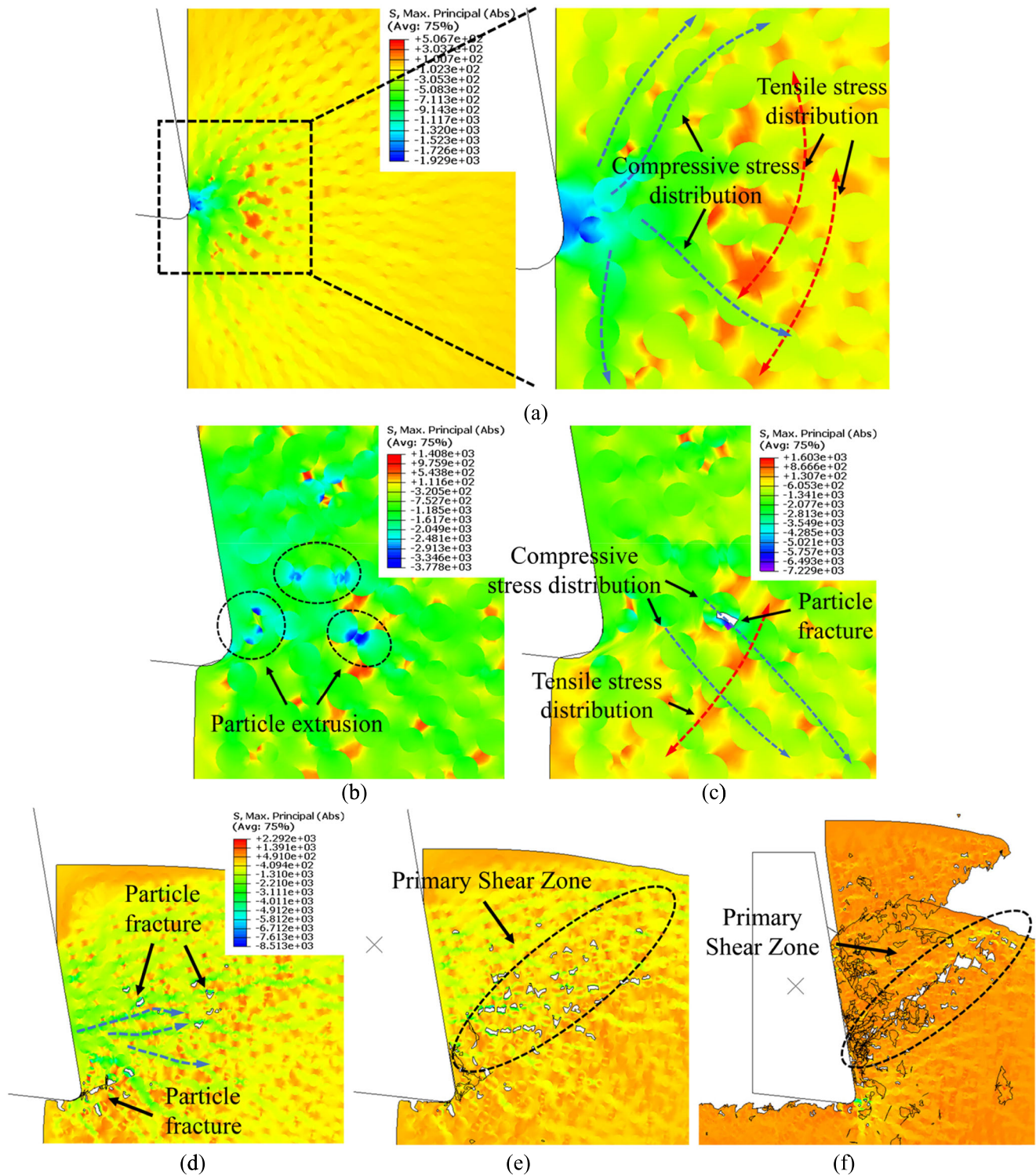
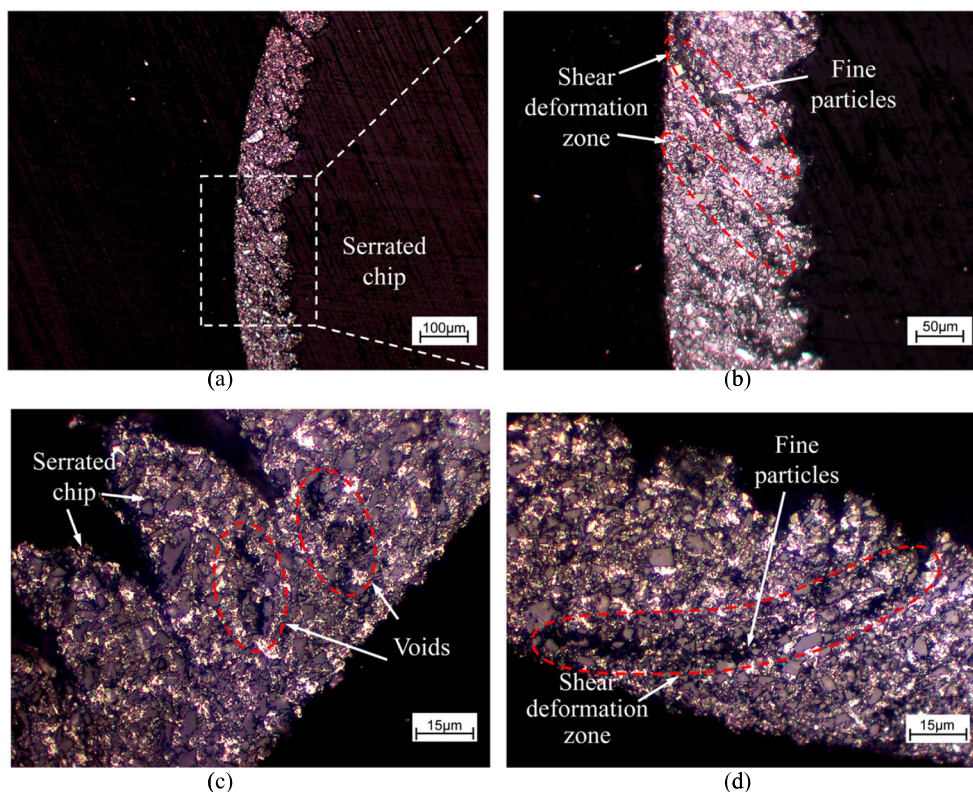


**Fig. 4** Max principal (abs) stress field during chip formation

caused by the shear deformation (Fig. 8d). Finally, as a result of the combined effects of matrix material local shear deformation and SiC particle fracture, the chips have a serrated shape (Fig. 8 e–f). The reasons for reticulation strain in particle-reinforced composites are multiple; the SiC particles distributed within the matrix produce a special microstructure;

the difference in elastic modulus between SiC and the matrix material causes localized inhomogeneous deformation of the material even under uniform loading; and according to the RF [43–47], stress relaxation occurs in the matrix material at the near interface due to thermal mismatch, resulting in a gradient distribution of dislocations and strains at the near interface,

Fig. 5 SiC<sub>p</sub>/Al chip morphology



and this inhomogeneous microstructure usually leads to strain localization during the deformation process. Therefore, taking into account the microstructural characteristics of the composites and the differences in the properties of the two phases materials, the composites are prone to non-uniform deformation at the microscopic level, resulting in a reticulated strain field, which has a relevant report in the RF [19–21]. The severe deformation of the primary shear zone causes particle fracture and interfacial debonding, while the deformation causes a local temperature increase that causes thermal

softening, which will cause more local deformation in the chip and make the chip appear serrated in shape.

### 3.3 Study of machined surface morphology

The simulated and experimental results of the machined surface morphology are shown in Figs. 9–10, and it can be observed from Fig. 10 that there are two major forms of damage on the machined surface: (a) surface pits or scratches, which are typically caused by particle fracture, debonding or pull-out, and particle pull-out or debonding that usually causes matrix tearing; (b) subsurface particle damage, which is primarily caused by tool-workpiece interaction. Compared to homogeneous materials, particle failure caused by cutting tool edge-particle interaction significantly degrades the surface morphology of SiC<sub>p</sub>/Al composites. Aside from the particle failure caused by tool-particle interaction, the extrusion of the flank face on the machined surface deforms the matrix material and causes residual strain on the machined surface, as shown in Fig. 9. Figure 10 also shows that some of the pits on the machined surface are re-covered by the deformed matrix (Fig. 10b–c). By comparing with the experimental results, the simulation results can predict the machined surface morphological defects.

The contact between the tool and the particle on the cutting path is random during machining. To investigate the interaction between the cutting tool edge and the particle, the relative positions between the cutting tool edge and the particle in

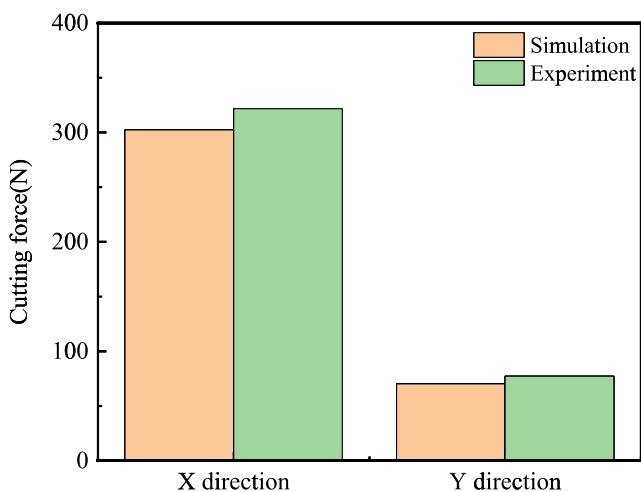
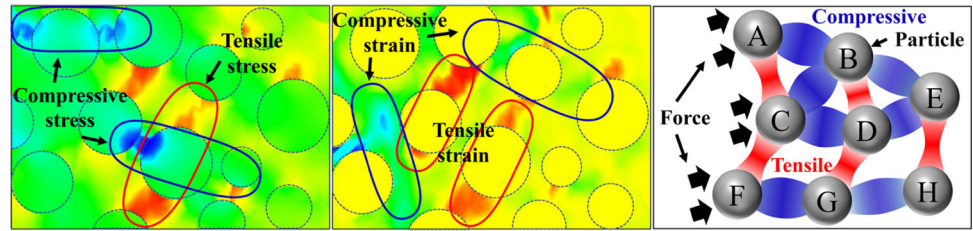


Fig. 6 Comparison of predicted and experimental cutting forces

**Fig. 7** Effect of the relative distribution of particles on stress and strain: **a** max principal (abs), **b** LE max principal (abs), and **c** relative position of particles



machining can be classified into three types (Fig. 11a): (a) the particle is located in the lower part of the cutting path (Type-I); (b) the particle is located in the cutting path (Type-II); and (c) the particle is located in the upper part of the cutting path (Type-III). Different relative positions between the cutting tool edge and the particles play different roles in particle failure, and particle failure can occur in both direct and indirect modes. When the particle is located in the lower part of the cutting edge (Type-I), the particle will be extruded by the cutting tool edge and pressed into the machining surface or broken to produce sub-surface damage, and a small part of the particle fragments will be removed with the chip to generate small pits or cavities (area A in Fig. 11b). In the case of particles located in the cutting path (Type-II), the particle tends to

be cut off by the cutting tool edge, and part of the particle fragments will be removed with the chip, resulting in large pits or scratches, while the rest of the particle fragments remain on the machined surface (area C in Fig. 11c). When the particle is in the upper part of the cutting path (Type-III), it is easily fractured by the rake face pushing, and the ploughing effect of the tool tends to cause the particle to be pulled out, which is accompanied by interface debonding or matrix tearing, and the majority of the particle fragments under this path will be removed with the chips, resulting in pits on the machined surface (area B in Fig. 11b). The fracture caused by contact between the tool and the particle is classified as direct failure, whereas the particle fracture caused by shear deformation of the matrix and mutual extrusion between the

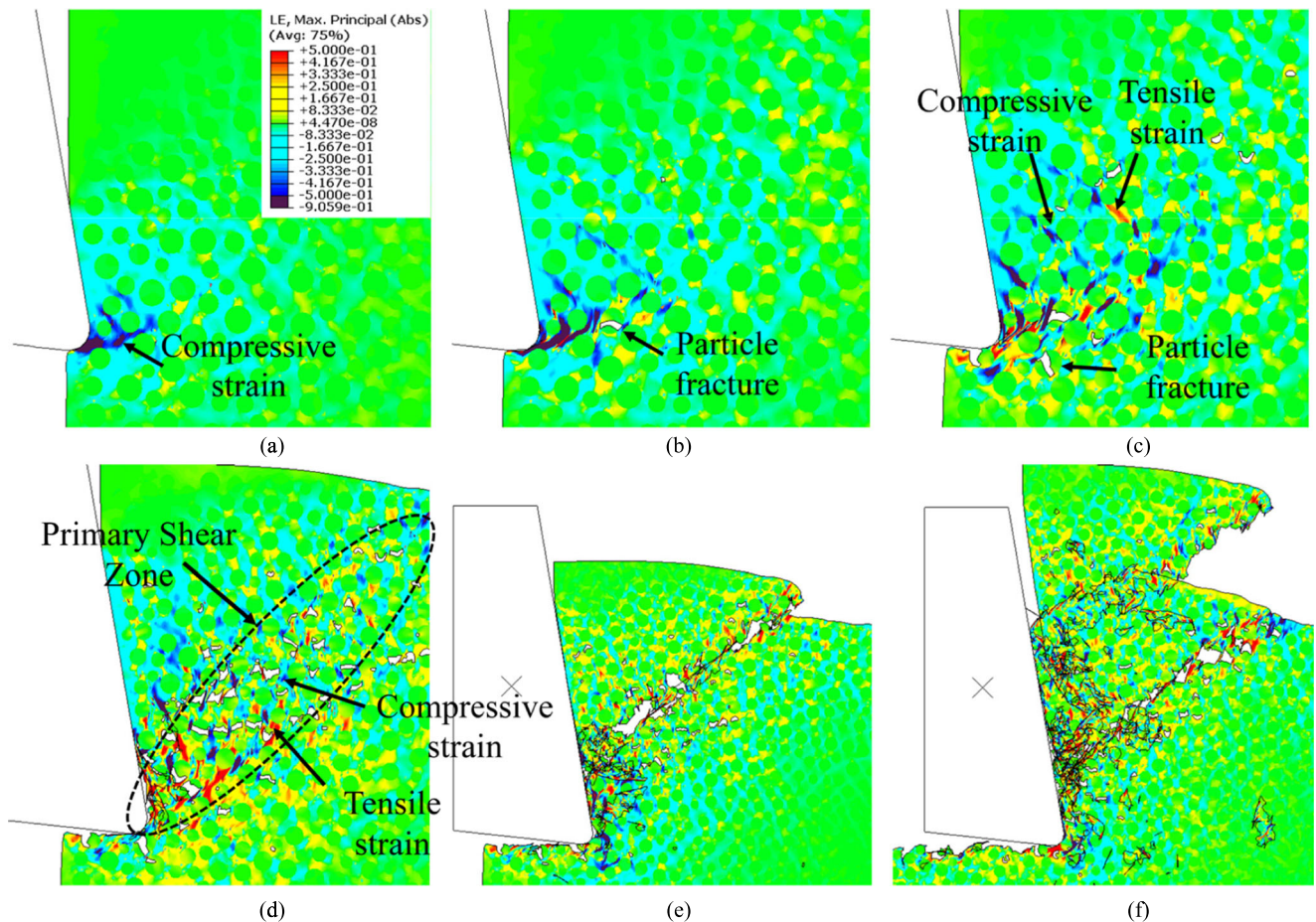
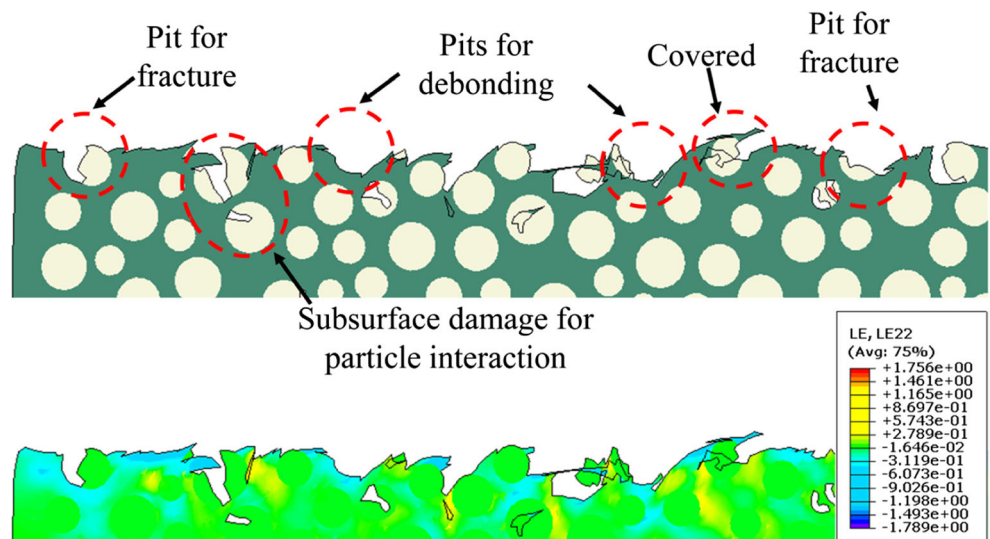


**Fig. 8** LE max principal (abs) strain field during chip formation



Fig. 9 Simulation morphology of machined surfaces



particles during machining is classified as indirect failure. The particle failure shown in area A of Fig. 11 is caused by direct contact under the Type-I path, in which the cutting tool edge extrudes the particle, causing it to fracture and expose the machined surface, actually damaging to the surface topography. In the Type-III path, where local plastic deformation of the workpiece causes the particles to extrude each other, leading to fracture or

debonding, cases of indirect contact that lead to particle failure are seen in areas B and D. As a result, the fine particles in the chip local deformation zone in Fig. 5 are caused by indirect damage. To summarize the preceding discussion, particle failure caused by interaction between the cutting tool edge and the particles is a significant factor of surface morphological defects in SiC<sub>p</sub>/Al composites.

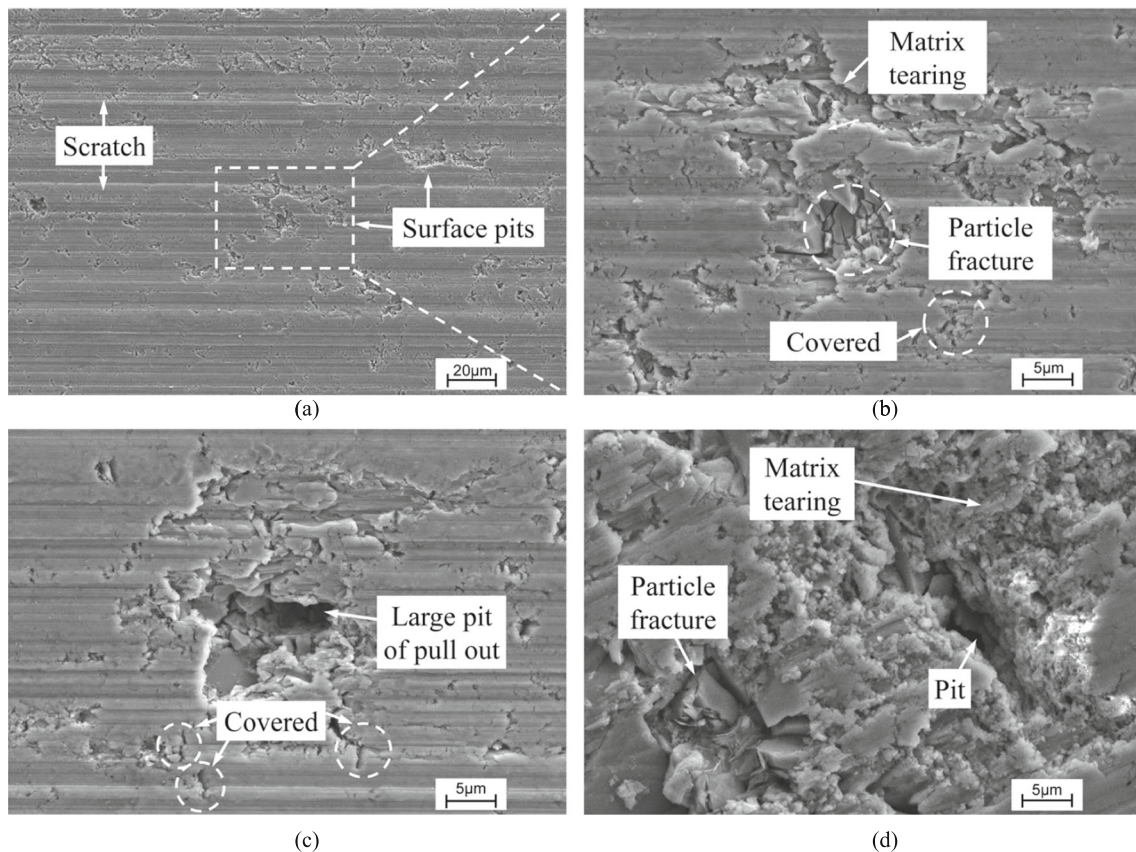


Fig. 10 Experimental morphology of machined surfaces

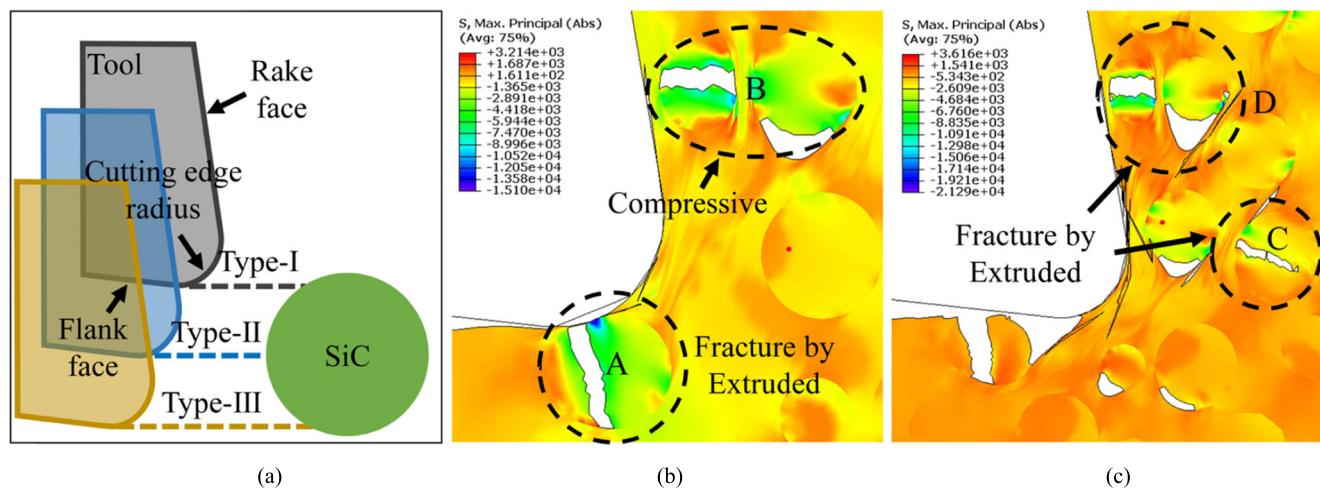


Fig. 11 Evolution of particle failure

## 4 Conclusion

To describe the microstructure of the composites, a multiphase  $\text{SiC}_p/\text{Al}$  composite cutting model considering material damage was developed in this paper. The chip formation process, stress-strain field, cutting force, and machining surface defects during machining were investigated, and the accuracy of the predicted results of the finite element model was validated by corresponding experiments. The major conclusions of this paper are as follows:

- (1) The chip formation of  $\text{SiC}_p/\text{Al}$  composites during machining includes local shear deformation of the matrix material and particle failure. The shear deformation of the matrix causes more frequent fracture of the particles in the primary shear zone, which makes the primary shear zone easier to destabilize causing the chip to exhibit a serrated shape.
- (2) The inhomogeneous microstructure of  $\text{SiC}_p/\text{Al}$  composites and the difference in material properties between the two phases lead to non-uniform stress-strain fields. The deformation of the matrix material is restrained by the particles, which results in a compound deformation in tensile and compression of the matrix in the local area during machining, where compressive deformation exists between the particles along the cutting speed direction and tensile deformation along the chip layer thickness direction.
- (3) Particle failure is influenced by the relative location of the cutting tool edge and the particle on the cutting path, and particle fracture can occur in both direct and indirect ways. The majority of fractured particles in the cutting path are caused by the direct way, while those in the main shear surface are caused by the indirect way.
- (4) Failed particles can cause defects on the machined surface such as pits, scratches, matrix tears, and subsurface

particle fracture, compromising the machined surface's integrity.

**Acknowledgements** The authors appreciate the support from the National Natural Science Foundation of China (Grant No. 51575289 and Grant No.51705270).

**Author contribution** This paper further explores the dynamic mechanisms of chip formation and particle failure in the machining of  $\text{SiC}_p/\text{Al}$  composites to provide some theoretical references for the optimization of composite design and cutting technology.

**Funding** This study is supported by the National Natural Science Foundation of China (Grant No. 51575289 and Grant No. 51705270).

**Data availability** The authors promise that all data are authentic.

**Code availability** ABAQUS finite element simulation software.

## Declarations

**Ethical approval** All authors agree with this article.

**Consent to participate** All authors voluntarily participated in the work of this paper.

**Consent to publish** All authors agree to the submission and publication of this paper.

**Conflict of interest** The authors declare no competing interests.

## References

1. Dandekar CR, Shin YC (2012) Modeling of machining of composite materials: a review. *Int J Mach Tools Manuf* 57:102–121. <https://doi.org/10.1016/j.ijmactools.2012.01.006>
2. Kim CS, Cho K, Manjili MH, Nezafati M (2017) Mechanical performance of particulate-reinforced Al metal-matrix composites

- (MMCs) and Al metal-matrix nano-composites (MMNCs). *J Mater Sci* 52(1):13319–13349. <https://doi.org/10.1007/s10853-017-1378-x>
3. Nicholls CJ, Boswell B, Davies IJ, Islam MN (2017) Review of machining metal matrix composites. *Int J Adv Manuf Technol* 90(9):2429–2441. <https://doi.org/10.1007/s00170-016-9558-4>
  4. Dabade UA, Joshi SS (2009) Analysis of chip formation mechanism in machining of Al/SiCp metal matrix composites. *J Mater Process Technol* 209(10):4704–4710. <https://doi.org/10.1016/j.jmatprotec.2008.10.057>
  5. Joshi SS, Ramakrishnan N, Ramakrishnan P (2001) Microstructural analysis of chip formation during orthogonal machining of Al/SiCp composites. *J Eng Mater Technol* 123(3):315–321. <https://doi.org/10.1115/1.1356026>
  6. El-Gallab MS, Sklad MP (2004) Machining of aluminum/silicon carbide particulate metal matrix composites: part IV. Residual stresses in the machined workpiece. *J Mater Process Technol* 152(1):23–34. <https://doi.org/10.1016/j.jmatprotec.2004.01.061>
  7. Ramesh MV, Chan KC, Lee WB, Cheung CF (2001) Finite element analysis of diamond turning of aluminium matrix composites. *Compos Sci Technol* 61(10):1449–1456. [https://doi.org/10.1016/S0266-3538\(01\)00047-1](https://doi.org/10.1016/S0266-3538(01)00047-1)
  8. Wang YF, Liao WH, Yang K, Teng XY, Chen WQ (2019) Simulation and experimental investigation on the cutting mechanism and surface generation in machining SiCp/Al MMCs. *Int J Adv Manuf Technol* 100(5–8):1393–1404. <https://doi.org/10.1007/s00170-018-2769-0>
  9. Wang X, Li YQ, Xu JK, Yu HD, Liu QM, Liang W (2020) Comparison and research on simulation models of aluminum-based silicon carbide micro-cutting. *Int J Adv Manuf Technol* 109(1):589–605. <https://doi.org/10.1007/s00170-020-05518-0>
  10. Fathipour M, Hamed M, Yousefi R (2013) Numerical and experimental analysis of machining of Al (20 vol% SiC) composite by the use of ABAQUS software. *Mater Werkst* 44(1):14–20. <https://doi.org/10.1002/mawe.201300959>
  11. Wang BB, Xie LJ, Chen XL, Wang XB (2016) The milling simulation and experimental research on high volume fraction of SiCp/Al. *Int J Adv Manuf Technol* 82(5–8):809–816. <https://doi.org/10.1007/s00170-015-7399-1>
  12. Li Y, Ramesh KT (1998) Influence of particle volume fraction, shape, and aspect ratio on the behavior of particle-reinforced metal-matrix composites at high rates of strain. *Acta Mater* 46(16):5633–5646. [https://doi.org/10.1016/S1359-6454\(98\)00250-X](https://doi.org/10.1016/S1359-6454(98)00250-X)
  13. Ye TK, Xu YX, Ren J (2019) Effects of SiC particle size on mechanical properties of SiC particle reinforced aluminum metal matrix composite. *Mater Sci Eng A* 753:146–155. <https://doi.org/10.1016/j.msea.2019.03.037>
  14. Qin SY, Chen CG, Zhang GD, Wang WL, Wang ZG (1999) The effect of particle shape on ductility of SiC<sub>p</sub> reinforced 6061 Al matrix composites. *Mater Sci Eng A* 272(2):363–370. [https://doi.org/10.1016/S0921-5093\(99\)00503-1](https://doi.org/10.1016/S0921-5093(99)00503-1)
  15. Spowart JE, Miracle DB (2003) The influence of reinforcement morphology on the tensile response of 6061/SiC/25p discontinuously-reinforced aluminum. *Mater Sci Eng A* 357(1–2):111–123. [https://doi.org/10.1016/S0921-5093\(03\)00244-2](https://doi.org/10.1016/S0921-5093(03)00244-2)
  16. Teng XY, Chen WQ, Huo DH, Shyha I, Chao L (2018) Comparison of cutting mechanism when machining micro and nano-particles reinforced SiC<sub>p</sub>/Al metal matrix composites. *Compos Struct* 203:636–647. <https://doi.org/10.1016/j.compstruct.2018.07.076>
  17. Teng XY, Huo DH, Chen WQ, Wong E, Zheng L, Shyha I (2018) Finite element modelling on cutting mechanism of nano Mg/SiC metal matrix composites considering cutting edge radius. *J Manuf Process* 32:116–126. <https://doi.org/10.1016/j.jmapro.2018.02.006>
  18. Pramanik A, Zhang LC, Arsecularatne JA (2008) Machining of metal matrix composites: effect of ceramic particles on residual stress, surface roughness and chip formation. *Int J Mach Tools Manuf* 48(15):1613–1625. <https://doi.org/10.1016/j.ijmactools.2008.07.008>
  19. Dai LH, Ling Z, Bai YL (1999) A strain gradient-strengthening law for particle reinforced metal matrix composites. *Scr Mater* 41(3):245–251. [https://doi.org/10.1016/S1359-6462\(99\)00153-0](https://doi.org/10.1016/S1359-6462(99)00153-0)
  20. Ashby MF (1970) The deformation of plastically non-homogeneous materials. *Philos Mag* 21(170):399–424. <https://doi.org/10.1080/14786437008238426>
  21. Jung HK, Cheong YM, Ryu HJ, Hong SH (1999) Analysis of anisotropy in elastic constants of SiCp/2124 Al metal matrix composites. *Scr Mater* 41(12):1261–1267. [https://doi.org/10.1016/S1359-6462\(99\)00295-X](https://doi.org/10.1016/S1359-6462(99)00295-X)
  22. Dandekar CR, Shin YC (2009) Multi-step 3-D finite element modeling of subsurface damage in machining particulate reinforced metal matrix composites. *Compos Pt A-Appl Sci Manuf* 40(8):1231–1239. <https://doi.org/10.1016/j.compositesa.2009.05.017>
  23. Pramanik A, Zhang LC, Arsecularatne JA (2007) An FEM investigation into the behavior of metal matrix composites: tool-particle interaction during orthogonal cutting. *Int J Mach Tools Manuf* 47(10):1497–1506. <https://doi.org/10.1016/j.ijmactools.2006.12.004>
  24. Pramanik A, Zhang LC, Arsecularatne JA (2006) Prediction of cutting forces in machining of metal matrix composites. *Int J Mach Tools Manuf* 46(14):1795–1803. <https://doi.org/10.1016/j.ijmactools.2005.11.012>
  25. Pramanik A, Zhang LC (2017) Particle fracture and debonding during orthogonal machining of metal matrix composites. *Adv Manuf* 5(1):77–82. <https://doi.org/10.1007/s40436-017-0170-0>
  26. Kannan S, Kishawy HA, Deiab I (2009) Cutting forces and TEM analysis of the generated surface during machining metal matrix composites. *J Mater Process Technol* 209(5):2260–2269. <https://doi.org/10.1016/j.jmatprotec.2008.05.025>
  27. Christman T, Needleman A, Suresh S (1989) An experimental and numerical study of deformation in metal-ceramic composites. *Acta Metall* 37(11):3029–3050. [https://doi.org/10.1016/0001-6160\(89\)90339-8](https://doi.org/10.1016/0001-6160(89)90339-8)
  28. Finot M, Shen YL, Needleman A, Suresh S (1994) Micromechanical modeling of reinforcement fracture in particle-reinforced metal-matrix composites. *Metall Mater Trans A* 25(11):2403–2420. <https://doi.org/10.1007/BF02648860>
  29. Mishnaevsky L Jr, Derrien K, Baptiste D (2004) Effect of microstructure of particle reinforced composites on the damage evolution: probabilistic and numerical analysis. *Compos Sci Technol* 64(12):1805–1818. <https://doi.org/10.1016/j.compscitech.2004.01.013>
  30. Zhang JT, Liu LS, Zhai PC, Fu ZY, Zhang QJ (2007) The prediction of the dynamic responses of ceramic particle reinforced MMCs by using multi-particle computational micro-mechanical method. *Compos Sci Technol* 67(13):2775–2785. <https://doi.org/10.1016/j.compscitech.2007.02.002>
  31. Johnson GR, Cook WH (1983) A constitutive model and data for metals subjected to large strains, high strain rates and high temperatures. *Proc 7th Int Sympo Ballistics* 21:541–548
  32. Johnson GR, Cook WH (1985) Fracture characteristics of three metals subjected to various strains, strain rates, temperatures and pressures. *Eng Fract Mech* 21(1):31–48. [https://doi.org/10.1016/0013-7944\(85\)90052-9](https://doi.org/10.1016/0013-7944(85)90052-9)
  33. Liu JW, Cheng K, Ding H, Chen SJ, Zhao L (2018) Simulation study of the influence of cutting speed and tool-particle interaction location on surface formation mechanism in micromachining SiCp/Al composites. *Proc Inst Mech Eng Part C - J Eng Mech Eng Sci* 232(11):2044–2056. <https://doi.org/10.1177/0954406217713521>
  34. Zhou L, Huang ST, Wang D, Yu XL (2011) Finite element and experimental studies of the cutting process of SiCp/Al composites with PCD tools. *Int J Adv Manuf Technol* 52(5–8):619–626. <https://doi.org/10.1007/s00170-010-2776-2>

35. Hillerborg A, Mod er M, Petersson P-E (1976) Analysis of crack formation and crack growth in concrete by means of fracture mechanics and finite elements. *Cem Concr Res* 6(6):773–781. [https://doi.org/10.1016/0008-8846\(76\)90007-7](https://doi.org/10.1016/0008-8846(76)90007-7)
36. Su YS, Ouyang QB, Zhang WL, Li ZQ, Guo Q, Fan GL, Zhang D (2014) Composite structure modeling and mechanical behavior of particle reinforced metal matrix composites. *Mater Sci Eng A* 597(12):359–369. <https://doi.org/10.1016/j.msea.2014.01.024>
37. Zhang J, Ouyang QB, Guo Q, Li ZQ, Fan GL, Su YS, Jiang L, Lavernia EJ, Schoenung JM, Zhang D (2016) 3D microstructure-based finite element modeling of deformation and fracture of SiC<sub>p</sub>/Al composites. *Compos Sci Technol* 123:1–9. <https://doi.org/10.1016/j.compscitech.2015.11.014>
38. Wu Q, Xu WX, Zhang LC (2019) Microstructure-based modelling of fracture of particulate reinforced metal matrix composites. *Compos Pt B-Eng* 163(15):384–392. <https://doi.org/10.1016/j.compositesb.2018.12.099>
39. Kan Y, Liu ZG, Zhang SH, Zhang LW, Cheng M, Song HW (2014) Microstructure-based numerical simulation of the tensile behavior of SiC<sub>p</sub>/Al composites. *J Mater Eng Perform* 23(3):1069–1076. <https://doi.org/10.1007/s11665-013-0805-7>
40. Zorev NN (1963) Inter-relationship between shear processes occurring along tool face and on shear plane in metal cutting. *Int Res Prod Eng ASME* 49:42–49
41. Wang T, Xie LJ, Wang XB (2015) Simulation study on defect formation mechanism of the machined surface in milling of high volume fraction SiC<sub>p</sub>/Al composite. *Int J Adv Manuf Technol* 79(5–8):1185–1194. <https://doi.org/10.1007/s00170-015-6876-x>
42. Pen HM, Guo JH, Cao ZZ, Wang XC, Wang ZG (2018) Finite element simulation of the micromachining of nanosized-silicon-carbide-particle reinforced composite materials based on the cohesive zone model. *Nanotech Pre Eng* 1(04):40–45. <https://doi.org/10.1016/j.npe.2018.12.003>
43. Goh CS, Wei J, Lee LC, Gupta M (2007) Properties and deformation behaviour of Mg-Y<sub>2</sub>O<sub>3</sub> nanocomposites. *Acta Mater* 55(15):5115–5121. <https://doi.org/10.1016/j.actamat.2007.05.032>
44. Ashby MF, Johnson L (1969) On the generation of dislocations at misfitting particles in a ductile matrix. *Philos Mag* 20(167):1009–1022. <https://doi.org/10.1080/14786436908228069>
45. Dunand DC, Mortensen A (1991) On plastic relaxation of thermal stresses in reinforced metals. *Acta Metall Mater* 39(2):127–139. [https://doi.org/10.1016/0956-7151\(91\)90261-X](https://doi.org/10.1016/0956-7151(91)90261-X)
46. Kim CT, Lee JK, Plichta MR (1990) Plastic relaxation of thermoelastic stress in aluminum/ceramic composites. *Metall Mater Trans A* 21(2):673–682. <https://doi.org/10.1007/BF02671938>
47. Unterweger K, Kolednik O (2013) The local deformation behaviour of MMCs-an experimental study. *Z Metallkd* 96(9):1063–1068. <https://doi.org/10.3139/146.101141>

**Publisher's note** Springer Nature remains neutral with regard to jurisdictional claims in published maps and institutional affiliations.